How to cite: *Angew. Chem. Int. Ed.* **2020**, *59*, 13335–13340
International Edition: doi.org/10.1002/anie.202003759
German Edition: doi.org/10.1002/ange.202003759

Single-Molecule Magnets

Axial Elongation of Mononuclear Lanthanide Metallocenophanes: Magnetic Properties of Dysprosium- and Terbium-[1]Ruthenocenophane Complexes

Gabrielle M. Risica, Veacheslav Vieru, Branford O. Wilkins, Trevor P. Latendresse, Joseph H. Reibenspies, Nattamai S. Bhuvanesh, Gregory P. Wylie, Liviu F. Chibotaru, and Michael Nippe**

Abstract: *We report the first f-block-ruthenocenophane complexes **1** (Dy) and **2** (Tb) and provide a comparative discussion of their magnetic structure with respect to earlier reported ferrocenophane analogues. While axial elongation of the rare trigonal-prismatic geometry stabilizes the magnetic ground state in the case of Dy^{3+} and results in a larger barrier to magnetization reversal (U), a decrease in U is observed for the case of Tb^{3+}.*

Introduction

The development of molecular architectures to maximize the magnetic anisotropy of lanthanide (Ln) ions in discrete mononuclear molecules has recently celebrated significant breakthroughs.[1] Most prominent is the discovery of the family of single-molecule magnets (SMMs) based on dysprosocenium cations[2] which has led to molecules that are able to display magnetic hysteresis up to 80 K.[3] Systematic studies of lanthanide platforms remain a crucial aspect of the development of future SMMs and are vital to elucidating structure–function relationships and formulating new molecular design guidelines.[4] In this regard it is truly remarkable that the first mononuclear lanthanide SMM platform, Ishikawa's iconic sandwich complex $[TbPc_2]^-$ (Pc^{2-} = phthalocyanine),[5] has also greatly contributed to the field of switchable magnetic properties in SMMs. In detail, it was found that either one- or two-electron oxidation of monoanionic $[LnPc^R{}_2]^-$ species (Ln = Tb^{3+} or Dy^{3+}) resulted in a significant axial compression in the corresponding neutral or monocationic species due to decreased intramolecular Pc^R-Pc^R plane separations around the central square antiprismatic lanthanide ion.[6] Importantly, as a result of this axial compression of the crystal field, significant enhancements in the observed energy barrier to reorientation of the magnetization (*U*) were reported (Scheme 1).

Our group has a standing interest in studying Ln-[1]metallocenophanes and correlating changes in molecular structure with dynamic magnetic properties.[7] We have previously disclosed the first example of a Dy-[1]ferrocenophane complex, $[Li(thf)_4][DyFc_3Li_2(thf)_2]$ (Fc = $[(\eta^5\text{-}C_5H_4)_2Fe]^{2-}$) ($\mathbf{1_{Fc}}$),[8] which features an approximate trigonal prismatic coordination environment around the Dy^{3+} ion and exhibited SMM behavior with a *U* of 110 cm^{-1}. A comparative study of its terbium-analogue, $[Li(thf)_4][TbFc_3Li_2(thf)_2]$ ($\mathbf{2_{Fc}}$)[9] revealed

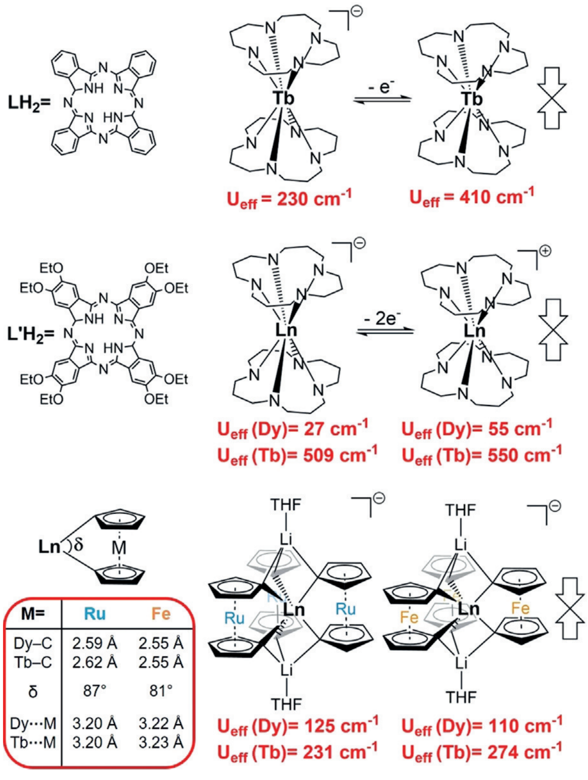

Scheme 1. Changes in *U* upon axial elongation/contraction in $[LnPc]^{-/0/+}$ and Ln-[1]metallocenophane complexes.

---

[*] G. M. Risica, B. O. Wilkins, T. P. Latendresse, Dr. J. H. Reibenspies, Dr. N. S. Bhuvanesh, Dr. G. P. Wylie, Prof. Dr. M. Nippe
Department of Chemistry, Texas A&M University
3255 TAMU, College Station, TX 77843 (USA)
E-mail: nippe@chem.tamu.edu

Dr. V. Vieru, Prof. Dr. L. F. Chibotaru
Theory of Nanomaterials Group, Katholieke Universiteit Leuven
Celestijnenlaan 200F, 3001 Leuven (Belgium)
E-mail: Liviu.Chibotaru@chem.kuleuven.be

Dr. V. Vieru
Current address: Maastricht Science Programme, Faculty of Science and Engineering, Maastricht University
Maastricht (Netherlands)

Supporting information and the ORCID identification number(s) for the author(s) of this article can be found under https://doi.org/10.1002/anie.202003759.

a larger value of U (274 cm^{-1}). This led us to suggest that there are analogies in magnetic properties between approximately C_3 symmetric Ln-ferrocenophanes and C_4 symmetric $[LnPc_2]^-$ complexes. In the present study, we are investigating the effect of axial elongation of Ln-[1]metallocenophanes on the dynamic magnetic properties. This structural elongation could be achieved by synthesizing the first lanthanide-[1]ruthenocenophane complexes, $[Li(thf)_4][DyRc_3Li_2(thf)_2]$ ($Rc = [(\eta^5\text{-}C_5H_4)_2Ru]^{2-}$) (**1**) and its terbium-analogue, $[Li(thf)_4][TbRc_3Li_2(thf)_2]$ (**2**). The larger ionic radius of the second-row transition metal ion Ru^{2+} ($r_{ion}(Ru^{2+}) \approx 0.72$ Å; $r_{ion}(Fe^{2+}{}_{ls}) = 0.61$ Å)[10] causes an increase in Cp-Cp-plane separations (by 0.17–0.20 Å) while maintaining a distorted trigonal prismatic coordination geometry around the Ln^{3+} ion. Interestingly, we find opposing trends in U values upon axial elongation for the Kramers ion Dy^{3+} (increase) and the non-Kramers ion Tb^{3+} (decrease) in going from $\mathbf{1_{Fc}}$ and $\mathbf{2_{Fc}}$ to **1** and **2**, respectively. This observation stands in direct contrast to the above discussed trends in magnetic properties of $[LnPc_2]^{-/0/+}$ complexes (Scheme 1, bottom) but can be rationalized by results from ab initio calculations.

Results and Discussion

The few examples of previously reported [1]ruthenocenophane complexes include solely diamagnetic species that feature coordination of 1,1′-ruthenocenyl moieties to zirconium and tin,[11] aluminum and gallium.[12] The structural differences between these complexes as compared to their [1]ferrocenophane analogs are generally larger Cp-Cp-plane separations as well as larger coordination angles (δ) around the chelated atom. Complexes **1** and **2** are prepared by adding a suspension of $DyCl_3$ or $TbCl_3$, respectively, in thf to a solution of 3.5 equivalents of $[Li_2(\eta^5\text{-}C_5H_4)_2Ru]\cdot(TMEDA)$[11] in thf (Scheme 2). After 20 hours, the pale-yellow solution is filtered and pulled to dryness. The crude product is washed with n-hexane, extracted in ether, and pulled to dryness. The resulting dark-yellow oil is dissolved in minimal amounts of thf and crystalized at room temperature via vapor diffusion of pentane to yield pale-yellow crystals of **1·thf** in 19% yields and **2·thf** in 10% yields. The diamagnetic Y^{3+} analogue (**3**) can be isolated in the same fashion with yields of 18%.

Complex **1·thf** and **2·thf** are isostructural, crystallizing in the monoclinic space group *Cc*, with one cocrystallized thf molecule per $[Li(thf)_4][LnRc_3Li_2(thf)_2]$ molecule (Table S1, S2 in the Supporting Information). The anionic $[LnRc_3Li_2(thf)_2]^-$ molecules (Figure 1) feature bonding of three dianionic ruthenocenophane moieties to the central Ln^{3+} (Ln = Dy, Tb) ion and two apical $[Li(thf)]^+$ units bound to the C1 atoms of each ruthenocenophane group. The geometry around the Ln^{3+} ion is best described as distorted trigonal prismatic (C_3) with a twist angle of 21 and 22° for the Dy^{3+} and Tb^{3+} analogues, respectively (Figure 2). The twist angles in **1** and **2** are significantly larger than the previously reported distortions for the ferrocenophane analogues $\mathbf{1_{Fc}}$ and $\mathbf{2_{Fc}}$ (8–11° distortion). The utilization of Ru^{2+} in **1** and **2** (instead of Fe^{2+} in $\mathbf{1_{Fc}}$ and $\mathbf{2_{Fc}}$) results in the desired increase in axial C_3–C_3 plane separation. The distance between the planes defined by the three C1 atoms bound to the central Ln^{3+} is 0.204 Å larger for **1** than for $\mathbf{1_{Fc}}$, and 0.181 Å larger for **2** than for $\mathbf{2_{Fc}}$. The magnitude of axial elongation in going from Ln-[1]ferrocenophanes to Ln-[1]ruthenocenophanes is much larger than the reported changes in N_4-N_4 separations in the family of $[LnPc^R{}_2]^{-/0/+}$ species (0.013 Å for $Pc_2Dy^{-/+}$; 0.031 Å for $Pc_2Tb^{-/+}$; 0.021 Å for $Pc_2Y^{-/0}$ and 0.005 Å for $Pc_2Y^{0/+}$) (Figure S1).[13] The elongation also causes wider average C_{Cp}-Ln-C_{Cp} angles (86.7° for **1** vs. 82.0° for $\mathbf{1_{Fc}}$; 86.5° for **2** vs. 81.1° for $\mathbf{2_{Fc}}$), and an elongation of the Ln−C bond lengths is also observed (2.592[11] Å for **1** vs. 2.545[5] Å for $\mathbf{1_{Fc}}$; 2.615[7] Å for **2** vs. 2.550[20] Å for $\mathbf{2_{Fc}}$). However, the larger C_3–C_3 plane separation in **1** and **2** (as compared to $\mathbf{1_{Fc}}$ and $\mathbf{2_{Fc}}$) results in smaller Ln···Ru distances (3.197[3] Å and 3.200[7] Å) than the Ln···Fe distances (3.222[5] Å and 3.230[4] Å) in $\mathbf{1_{Fc}}$ and $\mathbf{2_{Fc}}$.

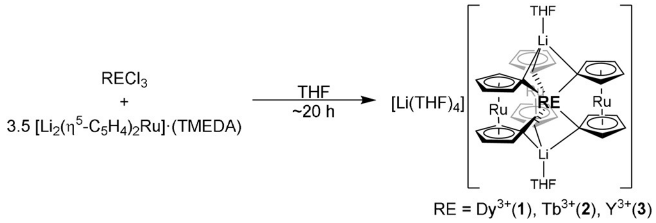

Scheme 2. Preparation of compounds **1**, **2** and **3**.

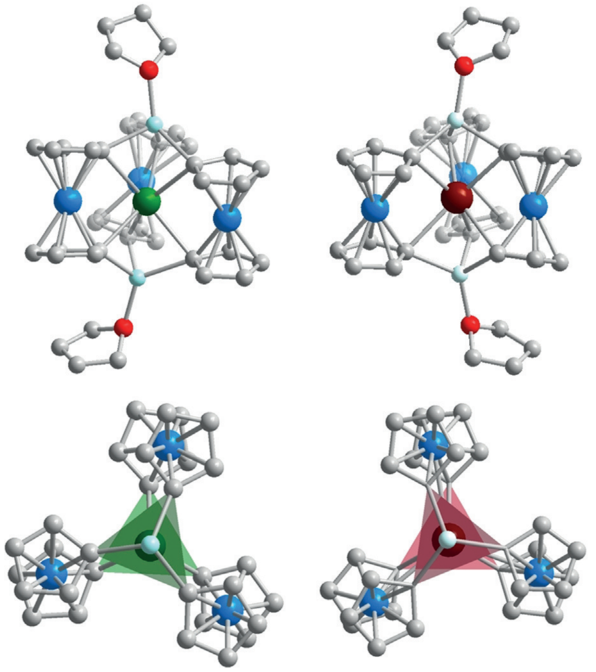

Figure 1. Top: Molecular structure of the monoanionic $[DyRc_3Li_2(thf)_2]^-$ molecule in crystals of **1·thf** (left) and $[TbRc_3Li_2(thf)_2]^-$ molecule in crystals of **2·thf** (right). Bottom: View down the Li-Ln-Li axis in **1·thf** (left) and **2·thf** (right) with coordinated thf molecules removed. Atoms are colored as follows: Dy = green, Tb = maroon, Ru = blue, Li = turquoise, C = grey, O = red. Hydrogen atoms, solvent molecules and counter-cation have been omitted for clarity.

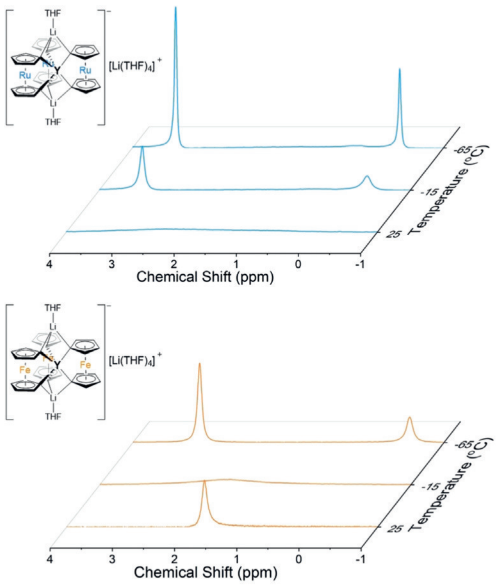

Figure 2. Variable temperature ^{7}Li-NMR spectra (thf-d_8) for **3** (left) and $\mathbf{3_{Fc}}$ (right) at 25, −15, and −65 °C.

Another interesting structural aspect of the new ruthenocenophane complexes **1** and **2** are the significantly shorter Li−C bond lengths (Δd(Li−C) = 0.041[15] Å for $\mathbf{1_{Fc}}$-**1**; Δd(Li−C) = 0.058[10] Å for $\mathbf{2_{Fc}}$-**2**). This shortening could indicate tighter bonding of Li^{+} in **1** and **2** (as compared to $\mathbf{1_{Fc}}$ and $\mathbf{2_{Fc}}$) and is possibly a consequence of reduced electrostatic repulsion between the apical Li^{+} ions and the central Ln^{3+} ion in **1** and **2**. In detail, axial elongation predictably leads to increased Ln⋅⋅⋅Li distances for Ln-[1]ruthenocenophanes (d(Ln⋅⋅⋅Li) = 2.768[12] Å for **1**; 2.764[14] for **2**; 2.718[5] Å for $\mathbf{1_{Fc}}$; 2.715[40] Å for $\mathbf{2_{Fc}}$) which reduces electrostatic Li^{+}⋅⋅⋅Ln^{3+} repulsion, increasing Li−C bond strengths, and elongating Ln−C distances further (see above).

To probe the relative strength of the Li−C interactions, variable temperature ^{7}Li-NMR studies were performed using a 1 M solution of **3** and $\mathbf{3_{Fc}}$ in thf-d_8 (Figure 2). At 25 °C, the spectrum for **3** features one broad, low intensity peak. As the solution is cooled, two sharp, well-defined peaks become visible at −15 °C and become sharper as the temperature is further reduced to −65 °C. The two signals are assigned to the metallocenophane-bound Li ions (3.31 ppm) and the counter cation [Li(thf)$_n$]$^{+}$ (0.30 ppm) species. In contrast to **3**, the spectrum of $\mathbf{3_{Fc}}$ features one sharp peak at 25 °C, one broad, low intensity peak at −15 °C, and two sharp, well-defined peaks become visible at −65 °C. These results indicate that (i) Li-ion exchange is dynamic in solution and that (ii) the apical lithium ions in **3** are less kinetically labile than in $\mathbf{3_{Fc}}$, further supporting stronger C−Li interactions in **3**.

The temperature dependence of the static magnetic properties of **1** and **2** were explored using direct current (dc) magnetic susceptibility measurements under an applied field of 1000 Oe in the temperature range of 2–300 K (Figures S2, S3). The $\chi_M T$ values at room temperature for **1** of 13.92 emu K mol^{-1} and for **2** of 11.75 at 300 K are close to the expected values for a single non-interacting Dy^{III} (14.17 emu K mol^{-1}: $^{6}H_{15/2}$, $S = 5/2$, $L = 5$, $g = 4/3$) and Tb^{III} (11.82 emu K mol^{-1}: $^{7}F_{6}$, $S = 3$, $L = 3$, $g = 3/2$) ion, respectively.[14] Upon decreasing the temperature, the value of $\chi_M T$ for both compounds remains relatively constant until reaching a temperature of 100 K, below which only a slight decrease is observed. A more significant decrease occurs at 12 K, until the value of $\chi_M T$ reaches a minimum of 9.39 emu K mol^{-1} for **1** and 9.80 emu K mol^{-1} for **2**, at 2 K. The decrease in the value of $\chi_M T$ at low temperatures could be attributed to weak intermolecular antiferromagnetic coupling, depopulation of Stark sublevels, or onset of dynamic effects. Since ab initio calculations reproduce the experimental $\chi_M T$ data well (see below), it is less likely that the decrease of $\chi_M T$ is due to dynamic effects. Magnetization vs. field measurements at variable temperatures (Figure S4–S7) show a maximum saturation of 5.19 μ_B for **1** and 4.63 μ_B for **2**, at 2 K. Expected saturation for a free, non-interacting Dy^{III} (10.6 μ_B) or Tb^{III} (9.0 μ_B) ion is significantly higher than attainable magnetization in the complex. Magnetization will decrease significantly in the presence of crystal field effects due to the lack of degeneracy in spin ground states and splitting of the m$_j$ levels. The fairly good overlap of M vs. H/T data, especially for **2**, suggests well isolated ground Kramers and pseudo doublets for both compounds, which is in agreement with their dynamic properties discussed below. Additionally, variable field magnetization measurements were conducted at 100 K (Figure S8, S9), showing an expected linear relationship and eliminating the possibility for ferromagnetic impurities in the crystalline sample measured.

The temperature dependence of the dynamic magnetic properties of **1** and **2** were probed using alternating current (ac) magnetic susceptibility measurements in the frequency range of 1–1000 Hz under zero applied dc field in a temperature range of 2–15 K for **1** (Figure S10) and 2–24 K for **2** (Figure S11). Both complexes display signals in the out-of-phase component of the molar ac susceptibility (χ_M'') within the frequency range, which is indicative of slow magnetic relaxation. The signal frequencies increase with increasing temperature in the high temperature regime, as expected for thermally activated relaxation processes, but show temperature independence at temperatures below 4 K, which is typically associated with the presence of quantum tunneling of the magnetization (QTM).[15] Application of static magnetic fields can reduce the relative contributions from QTM to magnetic relaxation via breaking of the degeneracy of m$_j$ states. Variable dc field, ac magnetic susceptibility measurements were performed at 8 K under an applied field in the range 0–10 000 Oe for **1** (Figure S12) and 0–3600 Oe for **2** (Figure S13). Under these conditions samples of **1** showed the presence of (at least) two closely overlapping signals which could not be fitted in a meaningful fashion. Compound **2** also displays signs of two relaxation processes upon the application of a 2400 Oe dc field in the temperature range of 14–24 K (Figure S14). In order to compare the magnetic properties of **1** and **2** in the absence of strong QTM contributions, diamagnetic dilution studies were performed. Diluted samples were prepared via co-crystallization of **1** or **2** with a stoichiometric excess of diamagnetic **3** (Dy:Y = 1:16; Tb:Y = 1:24). Within this diamagnetic matrix, both complexes display temperature dependence of their χ_M'' signals in the temperature range of 4–12 K for **1** (Figure 2, S15) and 8–32 K for **2** (Figure 3, S16). The magnetization relaxation times (τ) were extracted by fitting Cole–Cole plots (Figure S17–S21) using the generalized Debye equation [Eq. (S1), (S2); Table S5–S8).[16] At lower temperatures, the curves are seen to be symmetrical and semicircular, while in the higher temperature regimes, asymmetry is apparent in some data points, resulting in a tail-like feature at the end of the curve, for both complexes. This could be indicative of a second relaxation process moving into the experimental frequency range. However, due to the lack of data for the second process, the plots for both concentrated and dilute samples for were fit assuming a single process, excluding the points that strayed from the symmetric curve.

The temperature dependence of the relaxation times for concentrated and dilute samples is shown in the Arrhenius plots of **1** (Figure 4, left) and **2** (Figure 4, right). The absence of a temperature independent regime for the dilute samples indicates that diamagnetic dilution proved effective in reducing contributions from QTM for both complexes. These plots were fit to a linear equation [Eq. (S3)][17] to model only the Orbach processes in the high temperature limit, as well as to a full fit [Eq. (S4)][18] to account for Orbach, Raman and QTM processes across the full temperature range (Table S9, S10). The latter fits result in values of the effective magnetic barrier, U, of 126 cm^{-1} for **1** and 231 cm^{-1} for **2**. It is interesting to note that **1** displays a somewhat larger U value than its ferrocenophane congener $\mathbf{1}_{\mathbf{Fc}}$ (110 cm^{-1}) while that of **2** is smaller than the value for $\mathbf{2}_{\mathbf{Fc}}$ (274 cm^{-1}). These counterintuitive results are well in line with our computational results as is discussed below. We also note, that both LnRc$_3$ complexes act similarly to their ferrocenophane analogues, in that the concentrated and dilute samples show fairly similar barriers. The presence of slow magnetic relaxation would be expected to result in magnetic hysteresis at low temperatures. Variable field magnetization studies were conducted in a temperature range from 2–5 K using scan rates of 0.9 mT s^{-1} for **1** (Figure S22) and **2** (Figure S23). Solely complex **1** displays clear openings in its waist restricted hysteresis loops up to 5 K and both complexes reach magnetic saturation at 40000 Oe.

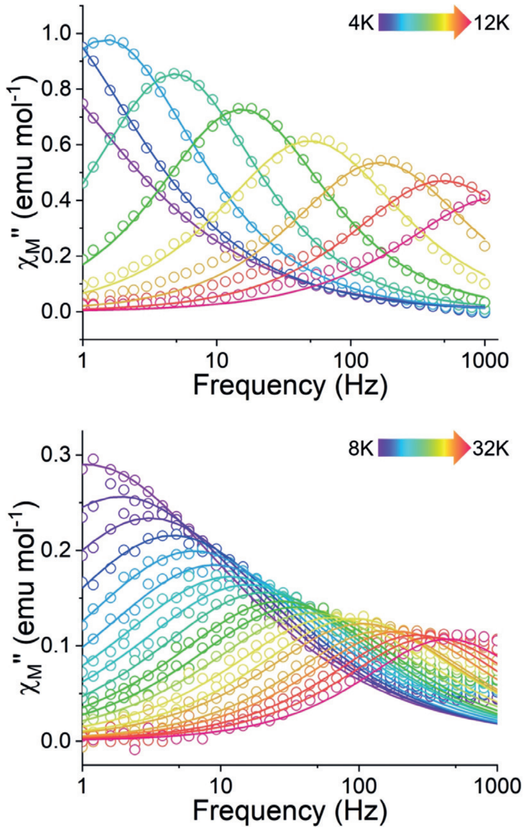

Figure 3. Temperature dependence of the out-of-phase component (χ_M'') of the ac susceptibility of a magnetically dilute sample of **1** (Dy:Y = 1:15.8, top) and **2** (Tb:Y = 1:24, bottom) under 0 Oe applied dc field in the temperature range 4–12 K and 8–32 K, respectively. Solid lines are the best fits to the experimental data, obtained with the generalized Debye model.

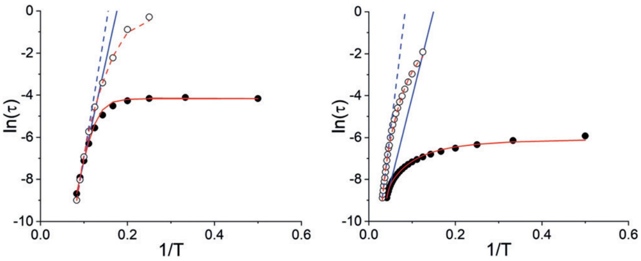

Figure 4. Arrhenius plot of magnetization relaxation time data for concentrated samples (solid circles) of **1** (left) and **2** (right) and magnetically dilute samples (open circles) of **1** (Dy:Y = 1:15.9) and **2** (Tb:Y = 1:24) in zero dc field. The solid and dashed red lines correspond to fits for all points for the concentrated and magnetically dilute sample, respectively. The blue lines correspond to the linear fit of the portion of the data that can be attributed to Orbach relaxation processes (Equation S3, S4).

The experimentally determined opposing trends in barrier heights upon axial elongation for Dy- (increase) and Tb-metallocenophanes (decrease) are further supported by computational analyses. Complexes **1** and **2** were calculated in two basis set approximations (Table S11). The active space of the CASSCF method included 9 electrons for complex **1** and 8 electrons for complex **2**, spanned by seven 4f orbitals. For compound **1**, 21 sextet, 128 quartet and 130 doublet states and for compound **2**, 7 septet, 140 quintet, 113 triplet and 123 singlet states were mixed by spin–orbit coupling within the module RASSI (Table S12, S13). Due to high computational cost, XMS-CASPT2 calculations were performed only on sextet states for **1** and septet states for **2**. Coordinated solvent molecules and counter-cation have been removed from the calculated fragment.

The energies of the Kramers doublets (KDs) of **1** and spin-orbital states of **2** along with their corresponding g-tensors are shown in Table 1. The calculated energies of the first and second excited states are larger for **1** (194 and 314 cm^{-1}) than for $\mathbf{1}_{\mathbf{Fc}}$ (180 and 236 cm^{-1}) while those of **2** (310 and 593 cm^{-1}) are smaller than in $\mathbf{2}_{\mathbf{Fc}}$ (343 and 649 cm^{-1}). This trend mirrors the above described experimentally determined trends in U values. Figure 5 shows the calculated structure of

Table 1: Energy and g-tensors of low-lying Kramers doublets for Dy center (**1**) and spin-orbital states for Tb center (**2**).

XMS-CASPT2/SO-RASSI Basis Set 2[a]		**1**	**2**
Energy [cm^{-1}]		0	0
		193.9757	0.0003
		313.6876	310.2557
		425.2105	310.2609
		556.8360	593.2008
		741.4731	593.4615
		929.1730	781.4962
		1053.1066	828.0393
			920.2413
			925.5532
			979.0890
			990.2700
			1007.2536
1	g_x	4.29×10^{-5}	0
	g_y	1.91×10^{-4}	0
	g_z	19.92	18.00
2	g_x	1.96×10^{-3}	0
	g_y	3.45×10^{-3}	0
	g_z	17.46	14.55
3	g_x	0.0544	0
	g_y	0.0640	0
	g_z	14.55	11.05
4	g_x	0.0455	–
	g_y	0.1240	–
	g_z	12.55	–

[a] Table S11 defines employed basis set.

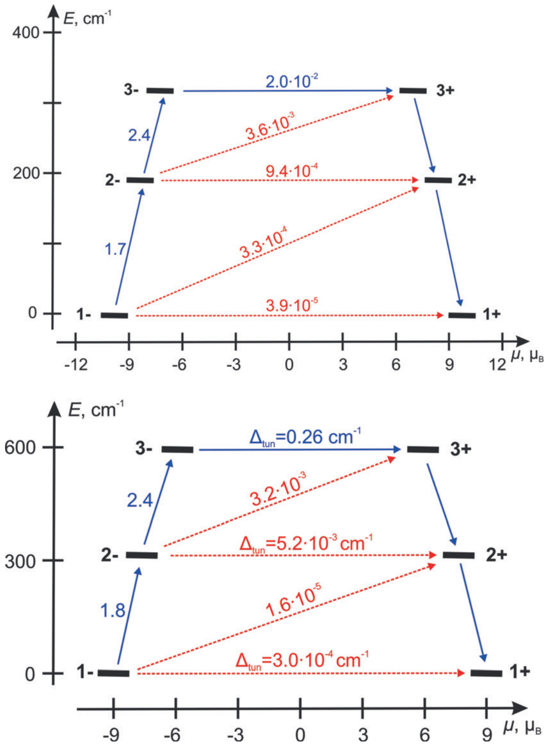

Figure 5. Low-lying levels and magnetization blocking barrier for **1** (top) and **2** (bottom). Each state (horizontal thick black lines) is located according to its magnetic moment. The arrows show the transition between the states, whereas the numbers accompanying them are the average transition moments (μ_B). The blue arrows indicate the barrier to the blocking of magnetization.

the magnetization blocking barrier and suggests that relaxation would be expected to occur via the second excited state for both **1** and **2**, which would result in even larger *U* values than those experimentally observed.

Given that the relaxation is of thermally activated QTM (TA-QTM) type, it proceeds via the doublet *n* with the largest value of $P_n\Gamma_n$, where P_n is the Boltzmann population of the corresponding doublet and Γ_n is the tunneling relaxation rate. The latter is proportional to Δ^2_{tun}, which in the case of **1** is related to $g_{x^2}+g_{y^2}$, while in the case of **2** is proportional to the square of the intrinsic gap of the given pseudo doublet. The Boltzmann population is proportional to $e^{-E_n/kT}$. By using the g-factors values of doublet 2, 3 and 4 and their corresponding energies in complex **1** (Table 1), one obtains at $T=20$ K: $\Gamma_2/\Gamma_3=13$, $\Gamma_3/\Gamma_4=1200$ and $\Gamma_2/\Gamma_4=1.4\times10^4$. This shows that the TA-QTM relaxation proceeds via doublet 2 (the first excited doublet). Similar analysis done for complex **2** provides $\Gamma_2/\Gamma_3=2.7\times10^5$ and $\Gamma_2/\Gamma_4=1.9\times10^8$ at $T=20$ K, which shows that the relaxation at relatively low temperatures occurs via the first excited pseudo doublet.

Close inspection of the ab-initio calculated crystal-field (CF) parameters allows to rationalize the counter-intuitive trends in *U* upon axial elongation. The decrease of first order terms (B^0_2) in going from ferrocenophanes to ruthenocenophanes (Table S14) is a consequence of overall weaker crystal fields in the latter. However, for Dy^{3+} the axial CF parameters (B^0_4) are slightly larger in **1** than in $\mathbf{1_{Fc}}$ (Table S14). This is somewhat surprising but consistent with our experimental findings and indicates that ruthenocenophanes enforce a more axial crystal field than ferrocenophanes for Dy^{3+} and highlights the value of ab initio calculations in elucidating such subtle geometric effects. The difference in the barriers height of **1** and $\mathbf{1_{Fc}}$ complexes (ca 15 cm^{-1}) is small, but the relaxation time is three orders of magnitude larger in $\mathbf{1_{Fc}}$ than in **1** (Table S15). The larger angle between the main magnetic axes of the ground and 1st excited doublet (0.44° in $\mathbf{1_{Fc}}$ and 13° in **1**[19]) causes a larger transition magnetic moment matrix element connecting the opposite doublet components of the ground and 1st excited KDs (1− and 2+ in Figure 5) in **1** compared to $\mathbf{1_{Fc}}$[9] which causes smaller relaxation times in the former. In contrast, the Tb^{3+} ion ($m_j=\pm6$) experiences a slight decrease of its axial CF terms and a larger decrease in its trigonal term (B^3_4) in going from $\mathbf{2_{Fc}}$ to **2**. This is also consistent with the larger twist angle observed for **2**. The $\approx$40 cm^{-1} lower barrier in **2** (as compared to $\mathbf{2_{Fc}}$) is therefore consistent with reported trends upon elongation but can be more specifically tracked back to specific changes in the CF splitting.

Conclusion

In summary, the isolation of the first f-block-ruthenocenophane complexes allowed us to comparatively evaluate trends in the magnetic structures of Dy^{3+} and Tb^{3+} ions in rare trigonal prismatic coordination environments. Our structure-function relationship studies support the formulation that the increased axiality of the crystal field for Dy^{3+} in **1** (as compared to $\mathbf{1}_{\mathbf{Fc}}$) results in improved U values while the weaker crystal field (especially as manifested in the trigonal CF terms) for Tb^{3+} decreases U for **2** (as compared to $\mathbf{2}_{\mathbf{Fc}}$).

Experimental Section

Experimental details and computational methods, including synthetic protocol, crystallographic information, structure tables and magnetic characterization methods can be found in the provided supporting information. CCDC 1955959, 1955961, 1955962, and 1955955 (**1**, **2**, **3**, $\mathbf{3}_{\mathbf{Fc}}$) contain the supplementary crystallographic data for this paper. These data can be obtained free of charge from The Cambridge Crystallographic Data Centre.

Acknowledgements

M.N. is grateful for support of this project by the National Science Foundation (CHE-1753014) and general financial support through The Welch Foundation (A-1880). V.V. acknowledges the postdoctoral fellowship of Fonds Wetenschappelijk Onderzoek Vlaanderen (FWO, Flemish Science Foundation).

Conflict of interest

The authors declare no conflict of interest.

Keywords: f-block chemistry · inorganic · magnetization dynamics · organometallic · single-molecule magnet

---

[1] a) B. M. Day, F. S. Guo, R. A. Layfield, *Acc. Chem. Res.* **2018**, *51*, 1880 – 1889; b) F. S. Guo, A. K. Bar, R. A. Layfield, *Chem. Rev.* **2019**, *119*, 8479 – 8505.

[2] a) C. A. P. Goodwin, F. Ortu, D. Reta, N. F. Chilton, D. P. Mills, *Nature* **2017**, *548*, 439 – 442; b) F. S. Guo, B. M. Day, Y. C. Chen, M. L. Tong, A. Mansikkamaki, R. A. Layfield, *Angew. Chem. Int. Ed.* **2017**, *56*, 11445 – 11449; *Angew. Chem.* **2017**, *129*, 11603 – 11607; c) K. R. McClain, C. A. Gould, K. Chakarawet, S. J. Teat, T. J. Groshens, J. R. Long, B. G. Harvey, *Chem. Sci.* **2018**, *9*, 8492 – 8503.

[3] F.-S. Guo, B. M. Day, Y.-C. Chen, M.-L. Tong, A. Mansikkamäki, R. A. Layfield, *Science* **2018**, *362*, 1400 – 1403.

[4] a) M. Guo, J. Tang, *Inorganics* **2018**, *6*, 16; b) J. D. Rinehart, J. R. Long, *Chem. Sci.* **2011**, *2*, 2078; c) D. N. Woodruff, R. E. Winpenny, R. A. Layfield, *Chem. Rev.* **2013**, *113*, 5110 – 5148; d) L. Ungur, L. F. Chibotaru, *Inorg. Chem.* **2016**, *55*, 10043 – 10056.

[5] N. Ishikawa, M. Sugita, T. Ishikawa, S.-y. Koshihara, Y. Kaizu, *J. Am. Chem. Soc.* **2003**, *125*, 8694 – 8695.

[6] a) N. Ishikawa, M. Sugita, N. Tanaka, T. Ishikawa, S.-y. Koshihara, Y. Kaizu, *Inorg. Chem.* **2004**, *43*, 5498 – 5500; b) N. Ishikawa, M. Sugita, W. Wernsdorfer, *Angew. Chem. Int. Ed.* **2005**, *44*, 2931 – 2935; *Angew. Chem.* **2005**, *117*, 2991 – 2995; c) N. Ishikawa, Y. Mizuno, S. Takamatsu, T. Ishikawa, S.-y. Koshihara, *Inorg. Chem.* **2008**, *47*, 10217 – 102019; d) S. Takamatsu, T. Ishikawa, S.-y. Koshihara, N. Ishikawa, *Inorg. Chem.* **2007**, *46*, 7250 – 7252.

[7] C. M. Dickie, A. L. Laughlin, J. D. Wofford, N. S. Bhuvanesh, M. Nippe, *Chem. Sci.* **2017**, *8*, 8039 – 8049.

[8] T. P. Latendresse, N. S. Bhuvanesh, M. Nippe, *J. Am. Chem. Soc.* **2017**, *139*, 8058 – 8061.

[9] T. P. Latendresse, V. Vieru, B. O. Wilkins, N. S. Bhuvanesh, L. F. Chibotaru, M. Nippe, *Angew. Chem. Int. Ed.* **2018**, *57*, 8164 – 8169; *Angew. Chem.* **2018**, *130*, 8296 – 8301.

[10] a) V. Petrusevski, S. Aleksovska, *Croat. Chem. Acta* **1991**, *64*, 577 – 583; b) R. D. Shannon, *Acta Crystallogr. Sect. A* **1976**, *32*, 751.

[11] U. Vogel, A. J. Lough, I. Manners, *Angew. Chem. Int. Ed.* **2004**, *43*, 3321 – 3325; *Angew. Chem.* **2004**, *116*, 3383 – 3387.

[12] a) J. A. Schachner, S. Tockner, C. L. Lund, J. W. Quail, M. Rehahn, J. Muller, *Organometallics* **2007**, *26*, 4658 – 4662; b) B. Bagh, G. Schatte, J. C. Green, J. Muller, *J. Am. Chem. Soc.* **2012**, *134*, 7924 – 7936.

[13] a) K. Katoh, Y. Yoshida, M. Yamashita, H. Miyasaka, B. K. Breedlove, T. Kajiwara, S. Takaishi, N. Ishikawa, H. Isshiki, Y. F. Zhang, T. Komeda, M. Yamagishi, J. Takeya, *J. Am. Chem. Soc.* **2009**, *131*, 9967 – 9976; b) T. Fukuda, S. Onodera, H. Watanabe, K. Shirasaki, A. Fuyuhiro, T. Yamamura, N. Ishikawa, *Dalton Trans.* **2017**, *46*, 12421 – 12424; c) H. Hückstädt, A. Tutass, M. Goeldner, U. Cornelissen, H. Homborg, *Z. Anorg. Allg. Chem.* **2001**, *627*, 485 – 497; d) C. Loosli, S. X. Liu, A. Neels, G. Labat, S. Decurtins, *Z. Kristallogr. New Cryst. Struct.* **2006**, *221*, 135 – 141.

[14] G. A. Bain, J. F. Berry, *J. Chem. Educ.* **2008**, *85*, 532 – 536.

[15] D. Gatteschi, R. Sessoli, *Angew. Chem. Int. Ed.* **2003**, *42*, 268 – 297; *Angew. Chem.* **2003**, *115*, 278 – 309.

[16] Y. N. Guo, G. F. Xu, Y. Guo, J. Tang, *Dalton Trans.* **2011**, *40*, 9953 – 9963.

[17] R. Bagai, G. Christou, *Chem. Soc. Rev.* **2009**, *38*, 1011 – 1026.

[18] S. T. Liddle, J. van Slageren, *Chem. Soc. Rev.* **2015**, *44*, 6655 – 6669.

[19] L. Ungur, L. Chibotaru, *Phys. Chem. Chem. Phys.* **2011**, *13*, 20086 – 20090.

Manuscript received: March 12, 2020
Accepted manuscript online: May 4, 2020
Version of record online: May 27, 2020